Astron. Astrophys. 333, 1117–1129 (1998)

ASTRONOMY AND ASTROPHYSICS

Three-dimensional simulations of jets

G. Bodo[1,3], **P. Rossi**[1], **S. Massaglia**[2], **A. Ferrari**[1,2,3], **A. Malagoli**[3], **and R. Rosner**[3]

[1] Osservatorio Astronomico di Torino, I-10025 Pino Torinese, Italy (surname@to.astro.it)
[2] Dipartimento Fisica Generale, Universitá di Torino, I-10125 Torino, Italy (surname@ph.unito.it)
[3] Department of Astronomy & Astrophysics, University of Chicago, Chicago, IL 60637, USA (surname@oddjob.uchicago.edu)

Received 20 June 1997 /Accepted 18 February 1998

Abstract. We present three-dimensional direct numerical simulations of an hydrodynamical supersonic jet, comparing them to analogous results obtained in two dimensions. The differences seen between three-dimensional and two-dimensional jet evolution including faster evolution, enhanced mixing and larger jet momentum depletion, are interpreted in terms of specific physical differences between these two cases. We have identified two main physical differences: The first is the faster development of small-scale structures in three dimensions, through either the growth of linearly unstable non-axisymmetric (three-dimensional) modes or the non-linear cascade of energy to smaller scales; the second is the different scaling of volumes in the two cases. Based on our 2-D and 3-D results, we discuss the limitations of using two-dimensional simulations to capture the evolution of three-dimensional jets.

Key words: hydrodynamics – instabilities – turbulence – galaxies: jets –ISM: jets and outflows

1. Introduction

Within the past few years, thanks to the increasing power of available supercomputers, three-dimensional (3-D) direct simulations of hydrodynamic jets have become a reality; and many of these calculations have been aimed at the astrophysical problem of explaining the existence and morphology of observed galactic and extragalactic jets. Most of these calculations have focused on the astrophysical jet propagation problem: Norman & Balsara (1992) considered propagation through a transonic cross flow; the effects of precession have been explored by Cox, Gull, & Scheuer (1991); and, finally, the interaction of a jet with a cloud has been studied by Clarke (1993). However, the basic physics of such jets remains inadequately understood, and for this reason, a number of other authors have focused on the details of how such jets evolve. In particular, other works have dealt with the evolution of Kelvin-Helmholtz instabilities associated with such jets, both on the analytical end (viz., Bodo et al. 1996) and numerically (Norman & Hardee 1988; Hardee & Norman 1989; Hardee, Cooper Norman & Stone 1992; Hardee & Clarke 1992; Bodo et al. 1994, 1995; Hardee, Clarke, & Howell 1995; Bassett & Woodward 1995). Most such studies have focused on the evolution of jets in space, i.e., have considered the spatial evolution of a perturbation imposed at the left boundary of the computational domain, where the jet enters. For example, Hardee & Clarke (1992) and Hardee, Clarke & Howell (1995) have studied respectively Mach 3 and Mach 5 light jets, i.e., jets whose density is ten times lower than that of the ambient medium, using this approach; both papers studied the 3-D evolution of such jets.

Other authors have studied temporal jet evolution by using periodic boundary conditions at the longitudinal boundaries of the computational domain. Thus, in two recent papers (Bodo et al. 1994, 1995; hereinafter Paper I and Paper II) we studied the evolution of supersonic jets subject to Kelvin-Helmholtz instabilities by means of two-dimensional (2-D) numerical simulations. In Paper I we adopted a cylindrical configuration, and considered axisymmetric perturbations; in Paper II we considered instead a slab jet, and analyzed symmetric and antisymmetric perturbations; such perturbations may be considered analogs, respectively, of the pinching and helical modes of a cylinder. The focus of those papers was on the understanding of the interaction of the jet with the ambient medium, through the processes of momentum and energy deposition and entrainment of external material induced by the instability evolution. These processes can be very important in determining both the jet's dynamical evolution and its observational properties. The main limitation of the analyses presented in those papers was obviously their geometry: It is well-known that there are many more unstable modes in three dimensions than in two dimensions, and that the growth rates of the 3-D modes can predominate. Furthermore, it is generally understood that turbulence in two and three dimensions differs substantially, especially as far as its mixing properties are concerned. Thus, issues such as the rates of entrainment can be expected to differ in two and three dimensions.

Some of these issues have been addressed recently by Bassett & Woodward (1995), who have studied Mach 2 and Mach 4 jets in two dimensions, and Mach 2 jets in three dimensions; their analysis focuses on the jets' temporal evolution by using periodic boundary conditions at the longitudinal boundaries. We consider in this paper jets with somewhat larger Mach numbers

Send offprint requests to: G. Bodo

(of order 10), using the same temporal approach as Bassett & Woodward (1995) and as our earlier work (Papers I and II); and we focus here on the three-dimensional case. A more significant difference between the work presented here and earlier work is the somewhat larger spatial resolution of our calculations.

While the differences between two and three-dimensional jet evolution have been long recognized, it has been often argued that the evolution of a slab jet may give insight to the evolution of an actual 3-D jet because the antisymmetric mode of the slab may mimic the helical mode of the cylinder; indeed, the results of linear analysis for these two configurations are in good agreement. In fact, it was difficult to go beyond such arguments earlier because actual 3-D direct simulations were prohibitively costly in terms of computational resources (or in fact simply could not be carried out). One of the aims in this paper is to compare 3-D results with 2-D slab results in order to determine to what extent the above analogy actually applies.

The other obvious issue we address is the formation of small-scale structure in 3-D, and their role in modifying the mixing properties of the unstable jet, especially as far as material entrainment and momentum mixing with the ambient medium are concerned. Small-scale structure formation can occur in two distinct ways: First, it arises as a consequence of unstable high wavenumber (3-D) modes; second, it results from cascades to higher wavenumbers via nonlinear interactions. Our results shed some modest light on this issue.

One of the remaining limitations of our study is the still-substantial computational expense of properly-resolved 3-D calculations. For this reason, it remains difficult to explore as large a parameter space domain in 3-D as we have done earlier in 2-D; thus, the calculations presented here focus on only one value of the Mach number ($M = 10$) and on only two values of the ratio of ambient medium density to jet density ($\nu = 10^{\pm 1}$).

The plan of our paper is as follows: in the next Sect. 2, we describe the physical problem; our numerical scheme is described in Sect. 3; our results are presented in Sect. 4; and the summary and discussion of the results are given in Sect. 5.

2. The physical problem

The evolution of a 3-D jet is governed by the ideal fluid equations for mass, momentum, and energy conservation,

$$\frac{\partial \rho}{\partial t} + \nabla \cdot (\rho \mathbf{v}) = 0\,, \tag{1a}$$

$$\rho \left[\frac{\partial \mathbf{v}}{\partial t} + (\mathbf{v} \cdot \nabla)\mathbf{v} \right] = -\nabla p\,, \tag{1b}$$

$$\frac{\partial p}{\partial t} + (\mathbf{v} \cdot \nabla)p - \Gamma \frac{p}{\rho} \left[\frac{\partial \rho}{\partial t} + (\mathbf{v} \cdot \nabla)\rho \right] = 0 \tag{1c}$$

in Cartesian geometry; the fluid variables p, ρ and $\mathbf{v}$ are, as customary, the pressure, density, and velocity, respectively; Γ is the ratio of the specific heats. Thus, we ignore all loss mechanisms, including radiative losses.

The initial flow structure is a cylindrical jet in the 3-D domain $\{(0, D) \times (-R, R) \times (-R, R)\}$, described by a Cartesian coordinate system (x, y, z). The initial jet velocity is along the x-direction; its symmetry axis is defined by $(y = 0,\ z = 0)$ (Fig. 1). As in our previous papers, the interface between the jet and the surrounding material is not indefinitely sharp; instead, the jet interior and the ambient medium are separated by a smoothly varying velocity shear layer. The particular form for the initial jet velocity profile is thus

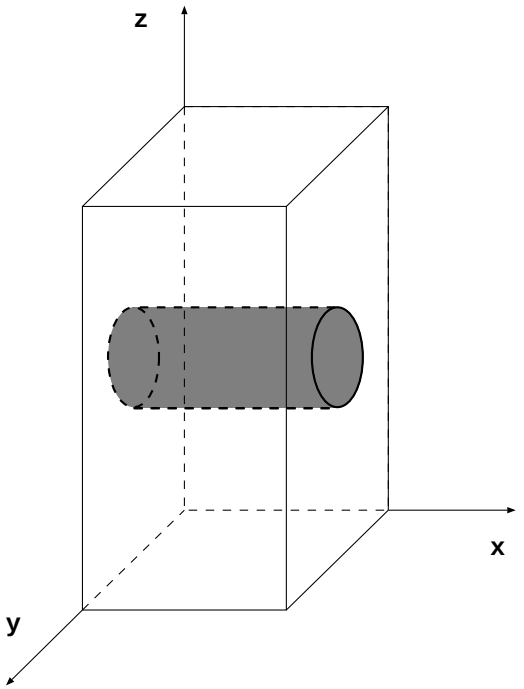

Fig. 1. Sketch of the integration domain

$$V_x(y, z) = V_0 \ \mathrm{sech} \left[\left(\frac{\sqrt{y^2 + z^2}}{a} \right)^w \right]\,,$$

where V_0 is the velocity on the jet axis, a is the initial jet radius, and m is a parameter controlling the interface (shear) layer width (typically, we set $w = 8$, which means that the ratio of the shear layer thickness to the jet radius of roughly 0.4). The initial spatial variation of density, $\rho(t = 0) = \rho_0(y, z)$, is identical to that of the initial jet velocity:

$$\frac{\rho_0(y, z; \nu)}{\rho_{\rm jet}} = \nu - (\nu - 1)\ \mathrm{sech} \left[\left(\frac{\sqrt{y^2 + z^2}}{a} \right)^w \right]\,,$$

where ν is the ratio of the density at $r = \sqrt{y^2 + z^2} = \infty$, ρ_∞, to that on the jet axis ($y = z = 0$) at $t = 0$, $\rho_{\rm jet} \equiv \rho_0(y = 0, z = 0)$. Finally, we assume that the jet is initially in pressure equilibrium with its surroundings; for this reason, we assume an initially uniform pressure distribution.

As in our previous papers, we will again focus on the mixing and entrainment properties of the jet as a consequence of the instability development. This analysis can be facilitated by following the evolution of a passive 'tracer' (i.e., a scalar field f which is advected without back-reaction by the fluid motions);

thus, we will also concurrently solve the scalar advection equation for f,

$$\frac{\partial f}{\partial t} + (\mathbf{v}\cdot\nabla) f = 0\,, \qquad (1d)$$

with initial conditions chosen in a way that allows to follow the jet material during its subsequent evolution:

$$f = \begin{cases} 1, & a < 1 \\ 0, & a > 1\,. \end{cases}$$

This initial configuration is then perturbed at $t = 0$. The particular functional form of this perturbation is such as to excite a wide range of modes. Thus, we impose a superposition of longitudinally periodic transverse velocities disturbances, using the functional forms

$$V_y(x,y,z) = \frac{V_{y,0}}{n_0}\,\mathrm{sech}\left(\frac{\sqrt{y^2+z^2}}{a}\right)^w \times \sum_{n=1}^{n_0} \sin(nk_0 x + \phi_n)\,, \qquad (2a)$$

$$V_z(x,y,z) = \frac{V_{y,0}}{n_0}\,\mathrm{sech}\left(\frac{\sqrt{y^2+z^2}}{a}\right)^w \times \sum_{n=1}^{n_0} \cos(nk_0 x + \phi_n)\,, \qquad (2b)$$

where $V_{y,0} = 0.005 V_0$ is the amplitude of the initial perturbation and $\{\phi_n\}$ are the phase shifts of the various Fourier components. These perturbations are thus a superposition of a fundamental, plus a number of its harmonics; and the functional form has been chosen in order to mainly excite the helical mode. This form also allows us to chose n_0 harmonics; one must then divide the initial perturbation by n_0 in order to properly normalize it. In the following, we have used the value $n_0 = 8$; this value is sufficiently small that the shortest wavelength mode excited can still be accurately followed in time (i.e., is adequately resolved) by our calculations.

The wavelength of the fundamental is set equal to the length of the computational domain; thus, $k_0 = 2\pi/D$, so that if we set $k_0 a = 0.2$, then $D = 10\pi a$. The shortest perturbation wavelength, $2\pi n_0/k_0$, is fixed by the maximum value of $n = n_0$, which - as already mentioned above - is set at $n_0 = 8$. It is essential to note that the fundamental (of wavelength D) does not necessarily coincide with the most unstable mode; the wavelength of the most unstable mode depends on the actual values of the parameters characterizing the initial state of the jet.

3. The numerical scheme

The basic equations (1a-d) have been integrated, as previously (Papers I and II), using a 3-D version of the Piecewise Parabolic Method (Colella & Woodward 1984). For a discussion of the merits of this method for this type of problem, we refer the reader to Bodo et al. (1995).

We cover our domain of integration ($0 \le x \le D$, $-R \le y \le R$, $-R \le z \le R$) by a $128 \times 256 \times 256$ grid (see Fig. 1). We have adopted free boundary conditions at the outer y and z boundaries ($y = \pm R$, $z = \pm R$); that is, the gradient of every variable is set to zero at these boundaries. These conditions, however, do not ensure perfect transmission at the boundaries. Therefore, in order to avoid spurious effects resulting from, viz., reflection at the computational boundaries, we have kept these boundaries as far away as possible from the jet surface by adopting a non-uniform grid in the y and z-directions. Thus, the central region of the domain, $-3a < y < 3a$, $-3a < z < 3a$, is covered uniformly by 150 grid points in the radial direction (with the jet itself initially occupying 50 grid points, at $t = 0$); at larger distances from the jet axis, both the y and the z mesh sizes increase according to the scaling laws $\Delta y_{j+1} = 1.02\Delta y_j$ and $\Delta z_{k+1} = 1.02\Delta z_k$, respectively. Thus, the y and z boundaries are located at $R = \pm 7$. In contrast, the boundary conditions in the x direction are periodic, and the grid along this direction is uniform.

As we have amply discussed in our previous papers, the main control parameters for this problem are the flow initial Mach number $M \equiv V_0/c_s$. where c_s is the sound speed on the jet axis at $t = 0$, and the density ratio ν between external density and jet density. Accordingly, our system of equations (1) has been non-dimensionalized by scaling lengths in units of the jet radius a, times in units of the sound crossing time over the jet radius, velocities in units of the sound speed, and density and pressure in units of their values on the jet axis at $t = 0$.

In addition, for comparing 3-D and 2-D results, we have repeated two slab (i.e., 2-D) calculations with the same parameters and with same grid setting as the 3-D calculations reported here: In this way, we minimize the effects of the grid from the comparison between 2-D and 3-D simulations. The comparison between these 2-D results with the results of the 2-D calculations reported in Paper II (in which case, for example, the grid has a smaller $x : y$ aspect ratio) show very good agreement, with the only noticeable difference being a slight difference in the onset time of the different phases of the temporal evolution.

4. Results

In order to facilitate our discussion of the results of the calculations, we first briefly review the relevant aspects of our previous results in the 2-D case, and then proceed to a detailed discussion of the 3-D calculations.

4.1. 2-D general jet evolution

In the analysis of our previous 2-D simulations of Kelvin-Helmholtz instabilities in supersonic jets (Bodo et al. 1994, 1995), we were able to distinguish four distinct stages which characterized the jet's evolution. The particulars of these four stages turned out to depend upon the values of the initial jet Mach number M and the density ratio ν; for example, the onset time of these stages, and both the morphological characteristics and the average physical properties of the asymptotic state of

the jet, depended on both M and ν. Different choices of the initial conditions, i.e. perturbation amplitudes and/or phase shifts, can change the temporal length of the initial stage, but leave the following evolution essentially unchanged. To recap:

1. *Stage 1 - Linear Phase*: The unstable modes excited by the initial perturbation grow in accord with linear theory. In the latter portion of this stage, the growth of the modes leads to the formation of internal shocks.

2. *Stage 2 - Acoustic Phase*: The growth of the internal shocks is accompanied by a global deformation of the jet, which drives shocks into the external medium. These shocks carry both momentum and energy away from the jet, and transfer these to the external medium. The onset of this stage occurs earlier for lower Mach number and denser jets, and later for higher Mach number and lighter jets. The beginning of this stage can be recognized by considering the temporal evolution of the jet longitudinal momentum,

$$\mathcal{P}_{\rm jet} \equiv \int_{-R}^{R} dy \int_{0}^{D} dx\ \rho f v_x\,, \qquad (3)$$

where we have used the scalar tracer f in order to maintain the distinction between jet and ambient fluid.

3. *Stage 3 - Mixing Phase*: As a consequence of the shock evolution, mixing between jet and the ambient medium begins. In Paper II we have quantitatively analyzed the beginning of this stage by introducing a quantity which we called the *tracer entropy*, whose exact definition can be found in Paper II. This quantity measures the departure of the tracer distribution from the initial form, and thus can tell us how much mixing between jet and external material has occurred. As for the previous stage, the onset of this stage also occurs earlier for lower Mach number and denser jets, and later for higher Mach number and lighter jets.

4. *Stage 4*: In this final state, the jet attains a statistically quasi-stationary state. This quasi-stationary state is different for heavy and light jets: While the former maintain some coherence as a jet-like velocity structure, the latter are essentially destroyed by the interaction with the ambient medium.

In the next subsections we will describe the corresponding evolution of the two 3-D cases we have examined, with an eye towards a detailed comparison to the 2-D jet evolution scenarios just described.

4.2. Case 1: The light jet ($M = 10$ $\nu = 10$)

The temporal evolution of the ($M = 10$ $\nu = 10$) 'light' 3-D jet, as compared with the corresponding evolution of a 'light' 2-D jet, is illustrated in the sequence of grey-scale images shown in Figs. 2 and 3: Fig. 2 shows the evolution of jet densities (note that in the 3-D case we show a 2-D cut in the xy plane), while Fig. 3 shows the corresponding evolution of the spatial distribution of the passive tracer, in the 2-D (right panels) and 3-D (left panels) cases.

One immediately notices that the 3-D jet evolves more quickly, and furthermore seems to show a more rapid development of small-scale structure, than the corresponding 2-D jet. A more precise measure of the latter feature can be gained by considering the two-dimensional power spectra (computed in the plane passing through the longitudinal jet direction). In Fig. 4 we show contour plots of such power spectra computed at $t = 8.8$ for the 3-D (upper panel) and the 2-D case (lower panel). The initial ($t = 0$) power spectra are strongly anisotropic, reflecting the anisotropy in the initial conditions. At the time shown in the figure the power spectra for the 3-D case are far more isotropic than in the 2-D case, i.e. the difference in Fig. 4 between the maximum longitudinal and transversal wavenumbers is $\sim 30\%$ for the 3-D case while reaches a factor of ~ 5 for the 2-D case. This indicates that the turbulent flow in the 3-D case is quickly isotropized, while the corresponding isotropization does not occur as quickly in the 2-D case. Secondly, comparing, in the two cases, the contours at 0.01 of the maximum value, we see that the growth of small scales in the longitudinal direction is distinctly smaller for the 2-D case than for the 3-D case.

In order to understand this behavior, it is useful to recall the results of linear theory. In Fig. 5 we show the growth rates obtained by solving the dispersion relation for the case of a cylindrical jet separated by a vortex sheet from the external medium (for detail see the Appendix). The upper panel corresponds to the present case (e.g., the light jet), solid lines represent the $m = 1$ helical mode, dashed lines represent the $m = 2$ mode and, finally, dashed-dotted lines represent the $m = 3$ mode. The different curves correspond to the ordinary and reflected modes and we see that all the modes with $m \geq 2$ have larger growth rates than the $m = 1$ helical modes. Now, as pointed out in Papers I and II, the 2-D numerical studies can follow the evolution of the pinching modes ($m = 0$) as well as of the helical modes ($m = 1$) for a cylindrical jet geometry.[1] However, the 2-D calculations cannot, as a matter of general principle, capture the evolution of higher order fluting ($m \geq 2$) modes, whose growth is in fact important for the solutions of the 3-D problem. We should therefore not be surprised to see more rapid development of small-scale structure in the three-dimensional case. The growth of non-axisymmetric modes in the simulations is illustrated in Fig. 6, where we show the transverse jet structure at $t = 4$. The two upper panels refer to this light jet case and show 2-D yz cuts of the spatial distributions respectively of density and of the passive tracer.

These results bear directly on the analysis of the various evolutionary stages in the 2-D jet case: In particular, it is evident that in the 3-D case, material mixing between the jet and the ambient medium begins early in the evolution (Fig. 2), as opposed to be delayed to Stage 3 in the 2-D case, in which entrainment occurs at times larger than roughly 14 crossing times.

[1] More precisely, we showed that the symmetric and antisymmetric modes of a slab jet correspond to the pinching ($m = 0$ modes) and helical modes ($m = 1$ modes) of a cylindrical jet.

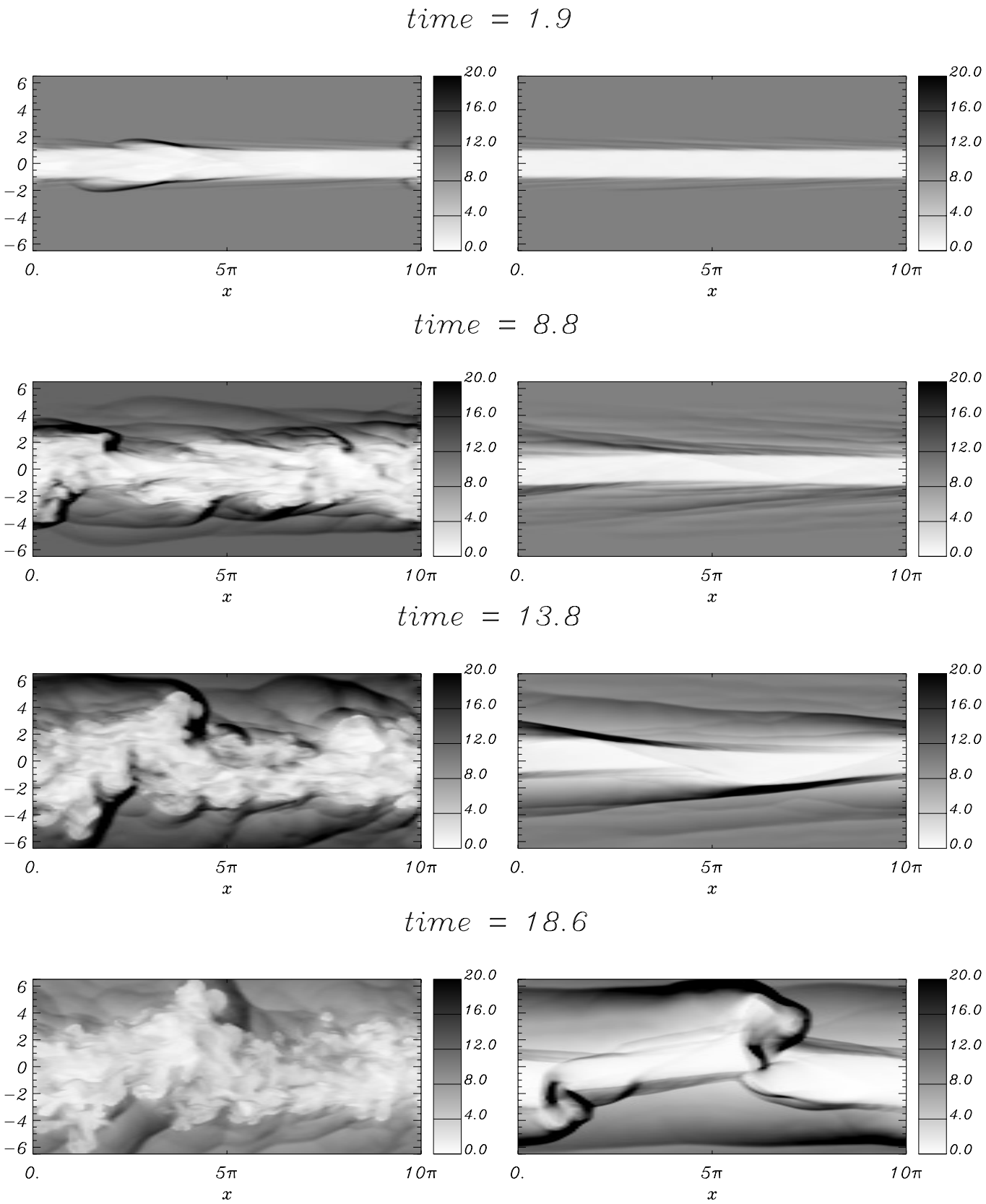

Fig. 2. Grey scale images of the density distributions for the light jet case ($\nu = 10$) at four different times. The left panels refer to the 3-D case and are cuts through the xy plane, the right panels refer to the 2-D slab case.

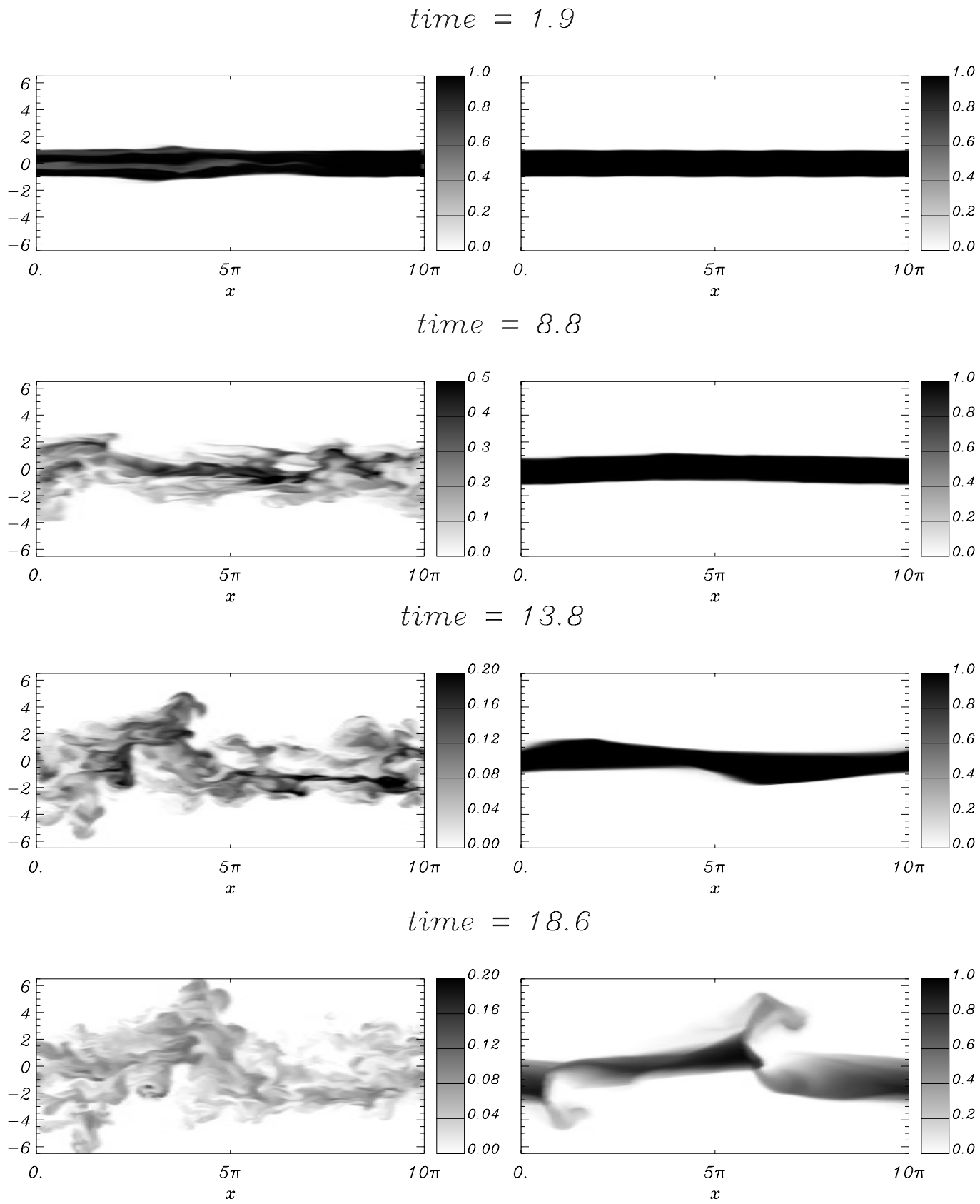

Fig. 3. Grey scale images of the tracer distributions for the light jet case ($\nu = 10$) at four different times. The left panels refer to the 3-D case and are cuts through the xy plane, the right panels refer to the 2-D slab case.

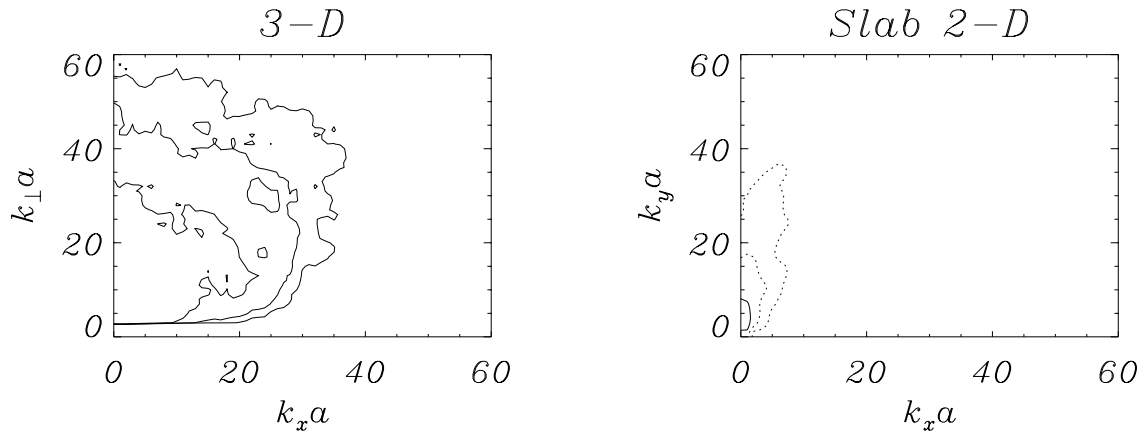

Fig. 4. Contour plot of the power spectrum in Fourier space, computed at $t = 8.8$. Solid contours are for levels larger or equal to 0.01 of the maximum value, dotted contours are for lower levels. In the 3-D case we show levels down to 0.01 of the maximum value, while in the 2-D case we show also two lower levels corresponding respectively to 0.003 and 0.001 of the maximum value.

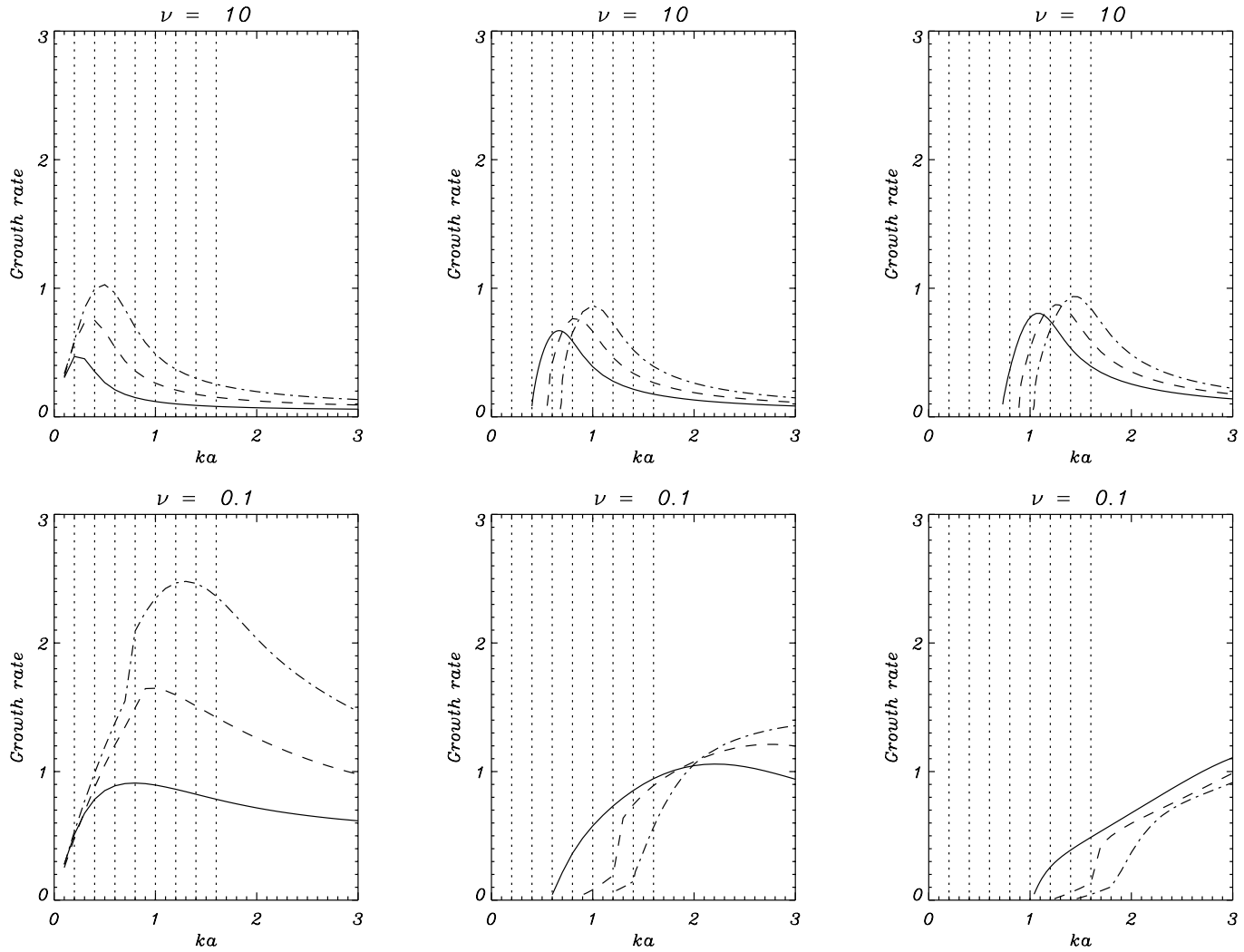

Fig. 5. Linear growth rates as functions of ka. The upper panels are for the light jet ($\nu = 10$) and the lower panels for the heavy jet ($\nu = 0.1$). Solid lines refer to the $m = 1$ modes, dashed lines to the $m = 2$ modes and dashed-dotted lines to the $m = 3$ modes. In each row the left panel refers to the ordinary mode, the middle panel to the first reflected mode and the right panel to the second reflected mode. The vertical dotted lines show the wavenumbers which are present in the initial perturbation.

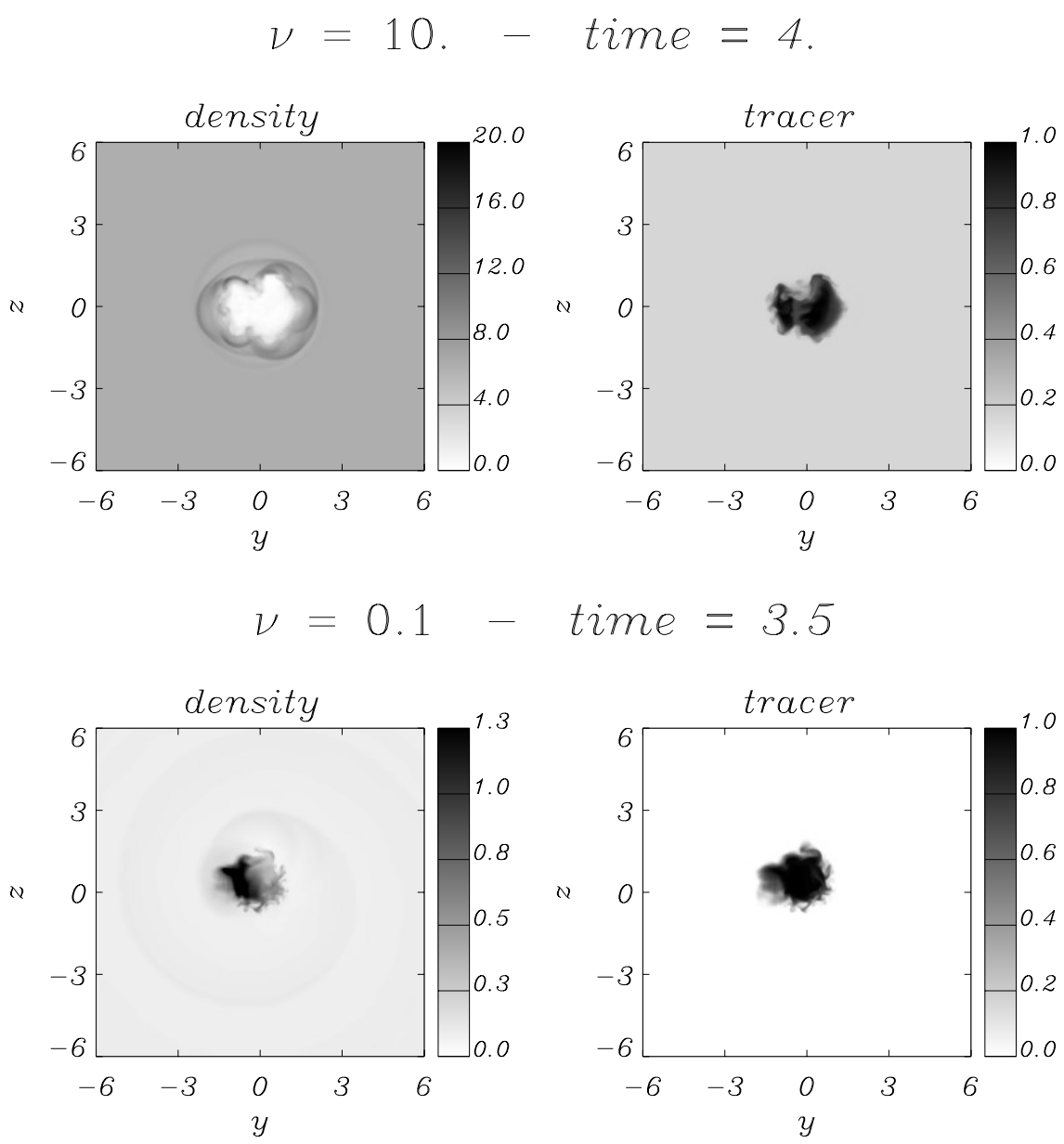

Fig. 6. Grey scale images of cuts through the yz plane of the density and tracer distributions. The upper panels refer to the 3-D light jet case ($\nu = 10$) and lower panels to the heavy jet case ($\nu = 0.1$).

This behavior is further illustrated by Fig. 7, which compares the temporal evolution of the total jet momentum $\mathcal{P}_{\rm jet}$, defined in Eq. (3) above, and of the jet entropy, for the 2 and 3-D cases: in both cases, it is evident that while mixing starts early in the 3-D case, such mixing is clearly delayed in the 2-D case. We interpret the absence of this delay in the 3-D case as a consequence of the rapid growth of small-scale motions, which we already discussed just above. Finally, we note that the asymptotic states for mixing of momentum are very similar in the 2 and 3-D cases, albeit that this state is reached at very different times for these two geometries.

We next observe that the generation of shocks within the jet and outside the jet can be observed in the 3-D case, as in the case of Stages 1 and 2 of the 2-D case. However, because of the rapid onset of mixing seen in the 3-D case, one cannot distinguish a clear separation of Stages 1, 2, and 3 in this higher-dimensional situation. That is, there is no clear separation of the onset of jet momentum mixing and onset of material mixing, as in the 2-D case; in the 3-D case, these processes proceed essentially simultaneously. We can understand this difference as follows: in the 2-D case, momentum transfer to the external medium is initiated by the driving of shocks into the ambient matter; and material mixing arises later, when small-scale motions begin to drive the mixing. In contrast, the rapid growth of small-scale motions in the 3-D case means that the material mixing will occur at roughly the same time as momentum is transfered to the external medium (by both external shocks and by the material mixing itself).

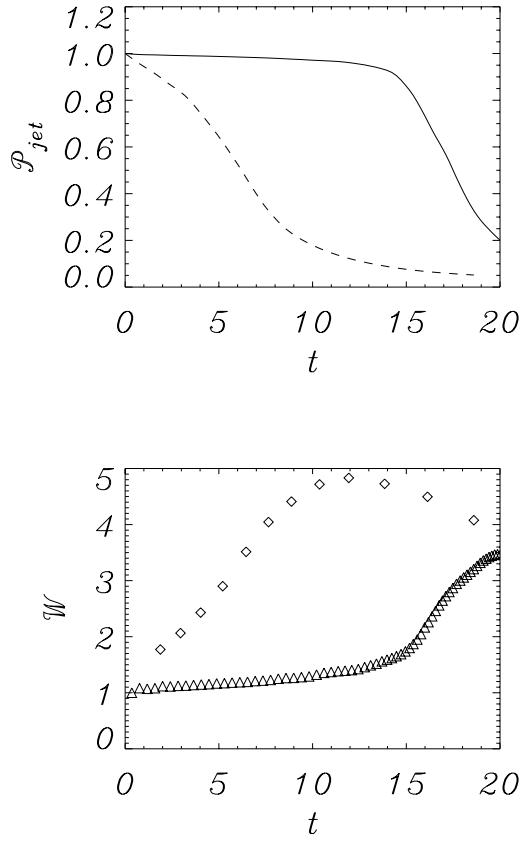

Fig. 7. Plot of the jet momentum $\mathcal{P}_{\rm jet}$ (upper panel) and the tracer entropy $\mathcal{W}$ (lower panel) as function of time, for the light jet case ($\nu = 10$). In the upper panel the solid curve refers to the slab (2-D) case and the dashed curve refer to the 3-D case. In the lower panel diamonds refer to the 3-D case, while triangles refer to the 2-D case.

Up to this point, we have implicitly assumed that the observed enhanced growth of small-scale structure in the 3-D case is a consequence of the presence of $m \geq 2$ modes, which are not present in the 2-D case, and whose growth rates are larger than those of the $m = 0$ and $m = 1$ modes. However, one may ask whether the enhanced growth of small-scale structure in the 3-D case could also be due to a more effective cascade of turbulent energy to larger wavenumbers in this case. While this question is very difficult to answer in general, we do note that our results point to the dominance of unstable $m \geq 2$ modes in mixing during at least the early periods of the 3-D jet evolution: As can be seen from Fig. 3, mixing of external material into the jet occurs at roughly 2 crossing times, well before there is much evidence for small-scale turbulent motions.

Finally, we note that one can observe features attributable to the helical mode (i.e., $m = 1$) in 3-D, as well as features attributable to the antisymmetric mode with the largest linear growth rate in 2-D (which is the 2-D counterpart to the 3-D helical mode), relatively late into the jet evolution: Such features can be recognized in both the 2 and 3-D tracer evolution grey-scale images at $t > 18$ crossing times. Thus, while the temporal evolution of the small-scale structures are very different in 2 and 3-D, the corresponding evolution of the largest-scale structures appear to be rather similar. An explanation for this behavior can be found in Hardee et al. (1995), who estimated the maximum displacement amplitudes for the various modes finding that while higher order modes have larger growth rates, the amplitudes that lower order modes can attain are larger, and therefore can show up at later times.

4.3. Case 2: the heavy jet ($M = 10$ $\nu = 0.1$)

The temporal evolution of the ($M = 10$ $\nu = 0.1$) 'heavy' 3-D jet is contrasted with the corresponding evolution of a 2-D 'heavy' jet in the sequence of grey-scale images shown in Figs. 8 and 9: Fig. 8 compares the evolution of jet densities in these two cases, while Fig. 9 compares the corresponding evolution of the spatial distribution of the passive tracer.

It is immediately apparent that the temporal evolution in this case is different than in the light jet case. First of all, one notices that the density evolution of the heavy 3-D jet is actually quite similar to that of the heavy 2-D jet: the external shocks appear at roughly the same time, as do the internal shocks; and the broadening of the jet itself is similar in both cases. When considering the tracer evolution instead, one notices that while the temporal increase in radial extent of the tracer is roughly similar in the 2 and 3-D cases (consistent with what one sees in the density images), the 3-D jet does appear to be significantly more mixed than the 2-D jet. That is, one sees a considerable amount of entrainment of external matter in the 3-D case, whereas there is comparatively little such entrainment in the 2-D case.

As in the previous case, the information provided by the linear analysis can be helpful for the interpretation of this case behavior. Hardee et al. (1995) pointed out that in addition to linear growth rate of the different modes, one has to consider also the maximum amplitude to wich each mode is allowed to grow and, with the simple assumption that the radial motions do not exceed the local sound speed, show that high order modes are allowed a smaller amplitude than low order modes. In the lower panels of Fig. 5 we can see the growth rates of linear modes for the present heavy jet case. We note that, while the $m \geq 2$ ordinary modes have larger growth rate than the $m = 1$ ordinary mode, the reflected modes with $m \geq 2$ have lower growth rates than those with $m = 1$ (in the range of wavenumbers that are effectively excited in this simulation). The $m = 1$ ordinary mode is however allowed a larger amplitude and therefore can be effective in determining the large-scale morphology of the jet in the non-linear regime, as in fact observed. In addition, we suggest that $m \geq 2$ ordinary modes, which are allowed a smaller maximum amplitude and which primarily perturbs a narrow region near the jet surface, have little consequences both on the morphology and on the mixing, while reflected (body) modes, which perturb the entire jet interior, can be more effective in driving the mixing in the non-linear stage of the evolution and in the low-scale range.

If this is the case, we would expect the early onset of rapid mixing we observed in the light jet case to be absent in the heavy jet case; and one would expect (in the 3-D case) to see mixing at small scales at roughly the same time as the growth

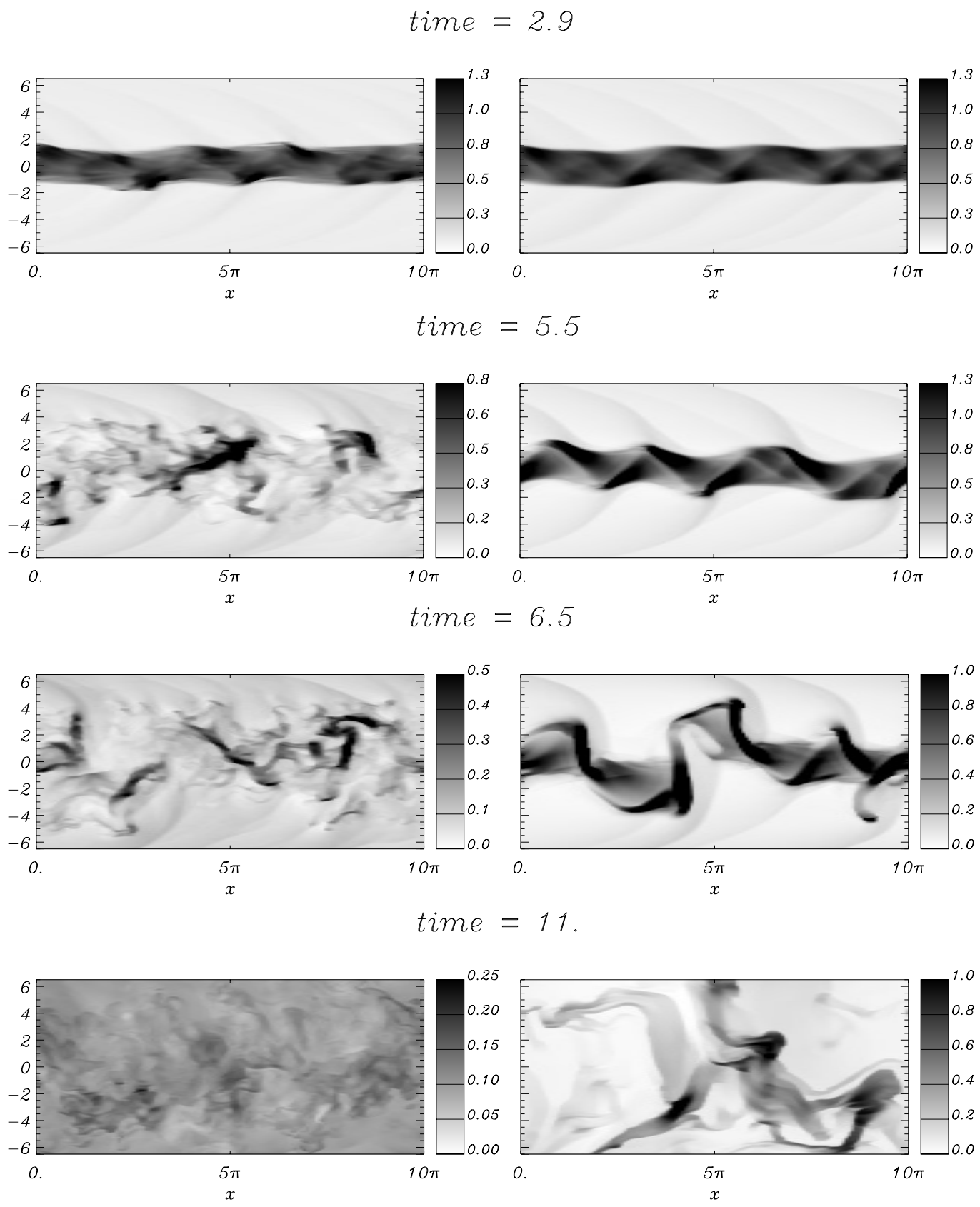

Fig. 8. Grey scale images of the density distributions for the heavy jet case ($\nu = 0.1$) at four different times. The left panels refer to the 3-D case and are cuts through the xy plane, the right panels refer to the 2-D slab case.

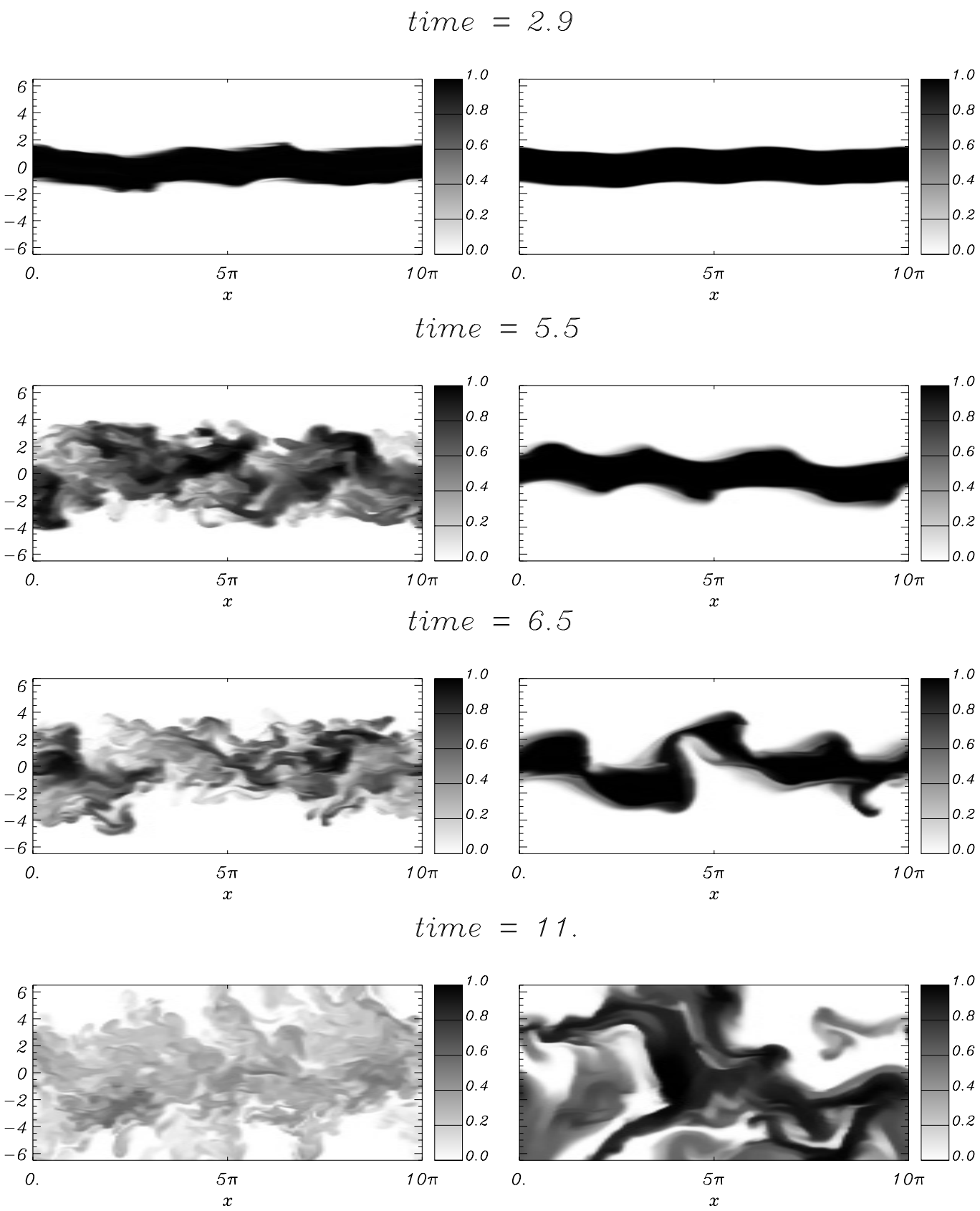

Fig. 9. Grey scale images of the tracer distributions for the heavy jet case ($\nu = 0.1$) at four different times. The left panels refer to the 3-D case and are cuts through the xy plane, the right panels refer to the 2-D slab case.

of large-scale jet deformation. Moreover, the ($m \geq 2$) modes do not exist in 2-D, and therefore one would expect to see only the effects of the analogs of the $m = 0$ and the $m = 1$ modes (i.e., the symmetric and the antisymmetric modes in the 2-D slab, respectively), which lead to larger-scale deformations of the jet. These expectations are precisely what is observed.

This picture is consistent with the temporal variation of total jet momentum (Eq. 3) for this case, shown in Fig. 10: in both the 2 and 3-D cases, we see that momentum mixing is delayed at the onset of the instability. However, one can see three differences between the 2 and 3-D cases:

(a) First, the onset of the rapid momentum exchange phase occurs much sooner for the 3-D case (at $t \sim 3$) than for the 2-D case (at $t \sim 5$). One can understand this as a simple consequence of the fact that the observed momentum exchange in the early evolution of the 3-D case is governed by the $m \geq 2$ modes, modes which do not exist for the 2-D case, but do for the 3-D case. In that case, the gradual steepening of the $\mathcal{P}_{\rm jet} = \mathcal{P}_{\rm jet}(t)$ curve for the 3-D case can be seen as a consequence of the exponential growth of these modes.

(b) Second, during the phase of rapid momentum exchange the rate is larger in the 3-D case than in the 2-D case (since the slope of $\mathcal{P}_{\rm jet} = \mathcal{P}_{\rm jet}(t)$ in the 3-D case is significantly steeper than in the 2-D case). This observation is most likely a consequence of geometry alone: That is, while the radial extent of the mixing is comparable in the 2 and 3-D cases (at least up to times of order 6 times the sound crossing time), the volume (and therefore mass) of the externally-mixed region differ substantially - in the 2-D case, this mass scales as the first power of the radial extent, while in the 3-D case, this mass scales as the square of the radial extent. Thus, the 3-D momentum exchange occurs more rapidly because more material is mixed within the same time span.

(c) Third, the extent to which the jet ultimately loses momentum (as indicated by the momentum carried in the asymptotic regime) is much larger for the 3-D case than for the 2-D case: Whereas the 3-D jet has lost almost 80% of its total momentum at $t \sim 12$, the 2-D jet has lost only roughly 40% of its total momentum, and appears to have reached a state of marginal stability; this latter state manifests itself when the heavy 2-D jet has entrained an amount of external material roughly equal in mass (or slightly more) than its own mass. In the case of the 3-D jet, the amount of external material entrained over the same radial extent is much larger: we estimate that the entrained material has a mass of order 5 times the 3-D jet mass. This estimate is consistent with the observed asymptotic value of $\mathcal{P}_{\rm jet} \sim 0.2$. Furthermore, the fact that the 3-D jet ultimately does not broaden as much in its velocity structure as does the 2-D jet can be accounted for by the same mechanism: for equal radial extents, the 3-D jet encompasses a far larger amount of external material than does the 2-D jet (Fig. 11).

Finally, we note that - as in the case of the light jet - we cannot easily distinguish the acoustic and mixing phases for the 3-D case.

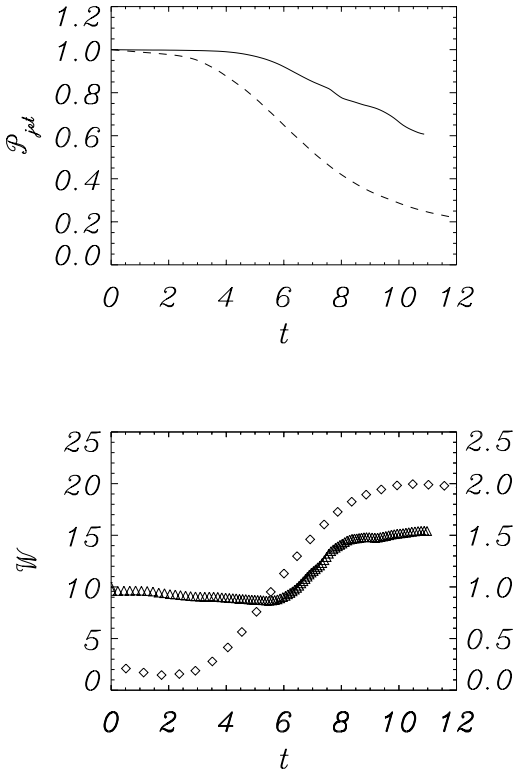

Fig. 10. Plot of the jet momentum $\mathcal{P}_{\rm jet}$ (upper panel) and the tracer entropy $\mathcal{W}$ (lower panel) as function of time, for the heavy jet case ($\nu = 0.1$). In the upper panel the solid curve refers to the slab (2-D) case and the dashed curve refer to the 3-D case. In the lower panel diamonds refer to the 3-D case, while triangles refer to the 2-D case; the ordinates on the left refer to the 3-D case and thos on the right to the 2-D case.

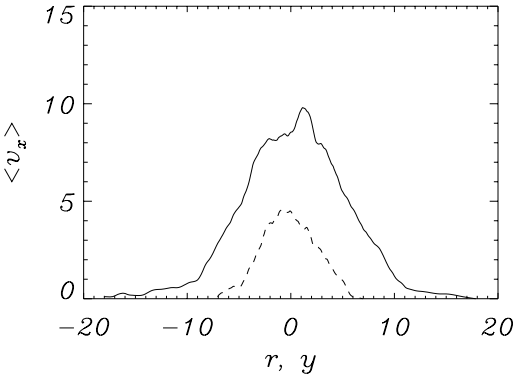

Fig. 11. Plot of the longitudinally averaged jet velocity $< v_x >$ as a function of the transverse coordinate y or r for the heavy jet case ($\nu = 0.1$) at $t = 11$. The solid curve is for the slab (2-D) case, while the dashed curve is for the 3-D case.

5. Summary and discussion

We have presented results of 3-D numerical simulations of the evolution of Kelvin-Helmholtz instabilities in supersonic ($M = 10$) hydrodynamic jets and have compared them with the analogous results obtained in 2-D; we considered both a light ($\nu = 10$) and an heavy jet ($\nu = 0.1$). The most evident differ-

ence between 2 and 3-D, independent of the contrast between jet and ambient density is the more rapid and effective mixing shown by the 3-D jet. This enhancement in mixing is evidently due to the much more rapid growth of small scale flow structures in the 3-D case.

The rapid development of small-scale structures is particularly evident in the light jet case ($\nu = 10$), in which these structures are already present in the very first phases of the evolution and result from the growth of linearly unstable higher-order ($m \geq 2$) fluting modes, which have growth rates larger than that of the helical mode. The presence of such modes leads to much faster evolution with respect to the 2-D case, and, for that reason, the asymptotic stage, in which the jet is virtually disrupted, is reached much sooner. The evolution of the heavy jet, in contrast, is not very different in 2 and 3-D, but even in this case, the global evolution is accelerated by the growth of small scale structures which enhance entrainment and momentum transfer.

The growth of small-scale structures can occur in two distinct ways: via either the growth of linearly unstable higher order ($m \geq 2$) non axisymmetric modes or a cascade to small scales through non-linear processes. An important issue to resolve is which of these two processes is dominant. As we have noted above, it is clear that it is the former process (growth of linearly unstable modes) that governs the early evolution of the light jet case, and it is also likely to be the responsible mechanism for the heavy jet, even though in this case the growth rates of non axisymmetric reflected modes are somewhat smaller. In the later jet evolution, however, it is difficult to say which of these two processes is the most important.

Another difference between 2 and 3-D jet evolution is the extent of radial jet broadening. This difference, which is most evident for the heavy jet (which also displays a much more profound momentum loss in 3-D) is largely due to the difference in volume scaling in 2 and 3-D. That is, in 2-D the entrained ambient mass scales linearly with radial extent, whereas in 3-D it scales quadratically.

An issue raised in the Introduction is the significance of 2-D results for understanding jet evolution. It is clear that the global evolution in 3-D appears to be much faster, and that the quantitative characteristics of the final state may be different; thus, 2-D calculations are not reliable for characterizing these aspects of jet evolution. However, we note that the evolution of the helical mode which largely determines the large-scale morphological features of a jet is actually well captured by the 2-D calculations. In fact, as pointed out by Hardee et al. (1995) this is the mode which should allow maximum amplitude in the non-linear regime. That is, 2-D calculations may be adequate for a partial description of the large-scale morphological jet evolution.

Finally, we note that the fast and disruptive instability evolution seen in our results again raise the long standing question as to how astrophysical jets can survive for such long scale lengths as shown by observations. Clearly new physical ingredients must be considered in more realistic simulations: one such ingredient is obviously the magnetic field, but radiative effects could also contribute to the observed stabilization of astrophysical jets (Rossi et al. 1997).

Acknowledgements. We would like to thank the Aspen Center for Physics, where some of this work was carried out. The calculations have been carried out on the Cray T3D at CINECA in Bologna, Italy. This work was supported in part by MURST in Italy, and by NASA and NSF grants to the University of Chicago.

Appendix

If we consider a fluid cylindrical jet separated by a vortex sheet from the external medium, we obtain from the linear analysis (Ferrari, Trussoni & Zaninetti 1981), the following dispersion relation:

$$\nu \frac{J'_m(ka\tau_i)H^{(1)}_m(ka\tau_e)}{J_m(ka\tau_i)H^{'(1)}_m(ka\tau_e)} = \frac{\tau_e}{\tau_i}\frac{(\phi - M)^2}{\phi^2} \quad ,$$

where J_n and $H^{(1)}_n$ are, respectively, the Bessel and Hankel functions of order m (azimuthal wave number), ϕ is a non-dimensional frequency, and

$$\tau_i^2 = k^2a^2\left[(\phi - M)^2 - 1\right] \quad ,$$

$$\tau_e^2 = k^2a^2\left[\phi^2\nu^2 - 1\right] \quad .$$

Growth rates represented in Fig. 5 are obtained by numerically solving this dispersion relation.

References

Bassett, G.M. & Woodward, P.R., 1995, ApJ, 441, 582
Bodo, G., Massaglia, S., Ferrari, A. & Trussoni, E., 1994, A&A 283, 655
Bodo, G.L., Massaglia, S., Rossi, P., Rosner, R., Malagoli, A., & Ferrari, A. 1995, A&A, 303, 281
Bodo, G.L., Rosner, R., Ferrari, A. & Knobloch, E., 1996, ApJ, 470, 797
Colella, P. & Woodward, P.R., 1984, J. Comp. Phys. 54, 174
Cox, C.I., Gull, S.F., & Scheuer, P.A.G., 1991, MNRAS, 252, 558
Ferrari, A., Trussoni, E., & Zaninetti, L. 1981, MNRAS, 196, 1051
Hardee, P.E. & Norman, M.L. 1989, ApJ, 342, 680
Hardee, P.E., Cooper, M.A., Norman, M.L. & Stone, J.M. 1992, ApJ, 399, 478
Hardee, P.E., & Clarke, D.A. 1992, ApJ, 400, L9
Hardee, P.E., Clarke, D.A. & Howell, D.A. 1995, ApJ, 441, 644
Norman, M.L. & Hardee, P.E. 1988, ApJ, 334, 80
Rossi, P., Bodo, G., Massaglia, S., Ferrari, A., 1997, A&A, 321, 672